Comprehensive analysis of TEM methods for LiFePO4/FePO4 phase mapping: spectroscopic techniques (EFTEM, STEM-EELS) and STEM diffraction techniques (ACOM-TEM)

Mu, X.; Kobler, A.; Wang, D.; Chakravadhanula, V. S. K.; Schlabach, S.; Szabo, D. V.; Norby, Poul; Kuebel, C.

Published in:
Ultramicroscopy

Link to article, DOI:
10.1016/j.ultramic.2016.07.009

Publication date:
2016

Document Version
Peer reviewed version

Comprehensive analysis of TEM methods for $LiFePO_4$/$FePO_4$ phase mapping: spectroscopic techniques (EFTEM, STEM-EELS) and STEM diffraction techniques (ACOM-TEM)

X. Mu[1,2], A. Kobler[1], D. Wang[1,3], V.S.K. Chakravadhanula[1,2], S. Schlabach[1,4], D.V. Szabó[1,4], P. Norby[5], C. Kübel[1,2,3]

1. Institute of Nanotechnology, Karlsruhe Institute of Technology, 76344 Eggenstein-Leopoldshafen, Germany

2. Helmholtz-Institute Ulm for Electrochemical Energy Storage (HIU), Karlsruhe Institute of Technology (KIT), 89081 Ulm, Germany

3. Karlsruhe Nano Micro Facility (KNMF), Karlsruhe Institute of Technology (KIT), 76344 Eggenstein-Leopoldshafen, Germany

4. Institute of Applied Materials, Karlsruhe Institute of Technology, 76344 Eggenstein-Leopoldshafen, Germany

5. Danmarks Tekniske Universitet (DTU), 4000 Roskilde, Denmark

Abstract

Transmission electron microscopy (TEM) has been used intensively in investigating battery materials, e.g. to obtain phase maps of partially (dis)charged (lithium) iron phosphate (LFP/FP), which is one of the most promising cathode material for next generation lithium ion (Li-ion) batteries. Due to the weak interaction between Li atoms and fast electrons, mapping of the Li distribution is not straightforward. In this work, we revisited the issue of TEM measurements of Li distribution maps for LFP/FP. Different TEM techniques, including spectroscopic techniques (energy filtered (EF)TEM in the energy range from low-loss to core-loss) and a STEM diffraction technique (automated crystal orientation mapping (ACOM)), were applied to map the lithiation of the same location in the same sample. This enabled a direct comparison of the results. The maps obtained by all methods showed excellent agreement with each other. Because of the strong difference in the imaging mechanisms, it proves the reliability of both the spectroscopic and STEM diffraction phase mapping. A comprehensive comparison of all methods is given in terms of information content, dose level, acquisition time and signal quality. The latter three are crucial for the design of in-situ experiments with beam sensitive Li-ion battery materials. Furthermore, we demonstrated the power of STEM diffraction (ACOM-STEM) providing additional crystallographic information, which can be analyzed to gain a deeper understanding of the LFP/FP interface properties such as statistical information on phase boundary orientation and misorientation between domains.

Keywords: Phase map; EFTEM; ACOM; $LiFePO_4$; Li-ion Battery

1. Introduction

Lithium (Li) batteries have been developed for more than two decades. They have plenty of commercial applications, which strongly impact human life. Lithium iron phosphate ($LiFePO_4$) is one of the most promising cathode materials for the upcoming next generation of Li ion batteries and has attracted great attention. Understanding the microscopic mechanism of the de/lithiation processes during electrical cycling is crucial to improve the performance of this material. Efforts to experimentally detect the lithium distribution in partially charged/discharged states at nanoscale

resolution are therefore essential. Many advanced techniques have been developed to obtain Li distribution maps: Scanning transmission X-ray microscopy (STXM) [1,2] or ptychography techniques [3–5] in synchrotron based setups were used to observe de/lithiation phase boundaries that started the discussion around its relationship to cycling current; Electron back scatter diffraction (EBSD) techniques in a scanning electron microscope (SEM) [6] was used to investigate the influence of the distance of particles to current collectors for the de/lithiation process.

Transmission electron microscopy (TEM) offers various sophisticated methods for $LiFePO_4$/$FePO_4$ (LFP/FP) phase mapping with high spatial resolution [6–16]. The mapping methods can be sorted into two families: one are spectroscopy methods based on the chemical information encoded in the energy spectra; the other are diffraction methods relying on the crystallographic information recorded in diffraction patterns or high resolution (HR)TEM images. In the first family of methods, electron energy loss spectroscopy (EELS) was one of forerunners to investigate the Fe-L and O-K edges, Li-K and Fe-M edges as well as the low-loss range resulting from interband transitions and plasma resonances [7,9,17–19]. The approach has been extended to 2 dimensions by combining EELS with scanning transmission electron microscopy (STEM) to obtain STEM-EELS spectral imaging (SI) and, for example, the differences in the O-K and Fe-L core loss spectra in LFP/FP have been used for phase mapping [8]. Alternatively, 2D phase mapping has been implemented by energy filtered transmission electron microscopy (EFTEM) spectral imaging, where the phase has been determined by measuring the chemical shift of the Fe-L_3 edge between the LFP and FP phases [11]. In the second family of methods, detection of the difference in lattice constants between LFP and FP has been adopted in the TEM to distinguish the phases. High resolution TEM imaging (HRTEM) and selected area electron diffraction (SAED) were applied to study the de/lithiation processes [13–16]. However, HRTEM provides only limited statistical information because of the small field of view. Automated crystal orientation mapping inside the TEM (ACOM-TEM), which was originally developed for orientation analysis of nanocrystalline and ultrafine grained materials [20,21], has been used to obtain LFP/FP phase maps over micrometers with a high resolution of 2 nm [12].

While the different spectroscopic and diffraction techniques have been applied to study the phase distribution in LFP/FP, so far, there is no convincing evidence indicating full agreement between the chemical information and the crystallographic information based phase maps because of a lack of comparison between the results gained from the two types of methods. In particular, the conclusions deduced from the STEM-EELS results by Honda et al. [8], where a core-shell FP/LFP de/lithiation structure was observed, is in discrepancy to the observation from the ACOM-TEM work from Brunetti et al. [12], where a Domino-Cascade model (de/lithiating particle by particle) was confirmed. The limited reliability of EFTEM based phase maps for samples with varying thickness has already been discussed by Sugar et al. [11], whereas for diffraction based analysis questions about the reliability arise due to the structural similarity of both phases and the corresponding small difference between the LFP and FP lattice constants, especially for higher index orientations. Therefore, in this work, we revisited the issue of TEM measurements of Li distribution maps for LFP/FP. We applied the different TEM techniques, including EFTEM-SI in the energy range from low-loss (interband transition, volume plasmon) to core-loss (Li-K and Fe-M edges, Fe-L edge) and ACOM-TEM for lithiation mapping of the same sample and sample location. This enabled a direct comparison of the results and, because of the strong difference in the detection process, provides a good measure for the reliability of the analysis. The maps obtained by all methods showed excellent agreements with each other, for ultra-microtomed sample with uniform thickness, proving the reliability of both the EFTEM/STEM-EELS maps (chemical information) and ACOM-TEM phase maps (crystallographic information). A

comprehensive comparison of all methods was given in terms of information content, dose level, acquisition time and signal quality. The latter three are crucial for the design of in-situ experiments with beam sensitive Li-ion battery materials. Furthermore, we demonstrated the power of ACOM-TEM with the additional crystallographic information, which can be analyzed to gain a deeper understanding of the LFP/FP interphase properties such as statistical information on phase boundary orientation and misorientation between domains.

2. Experimental

2.1 Sample preparation

The Electrode was prepared by mixing LFP nanoparticles with Super P carbon black and binder. The electrode was first charged to 4.0 V at 2 mA (ca. 1 C rate). It was then discharged for 30 min at 2 mA to reach ca. 50% lithiation state. In this state, the electrode was dismounted from the cell for further TEM specimen preparation.

Misleading results of EFTEM-SI can be caused by thick specimens. Therefore, in this work, we used ultramicrotomy for the sample preparation. Details are given in the supplementary information section 1 (SI.1). The average thickness of the active material (LFP/FP particles) in the specimen was measured by EFTEM thickness mapping to be around 0.6 λ (figure S 1) corresponding to ~80 nm.

2.2 ACOM-TEM

ACOM-TEM data was collected on a Tecnai F20 (Philips) operated at 200 kV in micro-probe STEM mode and equipped with a NanoMegas ASTAR system. For the data acquisition, spot size 8, gun lens 6, extraction voltage of 4.5 kV and 30 µm condenser (C2) aperture were used. The probe size was around 1.0-1.5 nm diameter with a convergence semi-angle of 0.8 mrad. The camera readout frequency was set to 100 fps (frames per second) for the diffraction pattern acquisition. The camera length was set to 100 mm. To minimize the influence of dynamic scattering, the electron beam was precessed with precession angle of 0.5°, which slightly broadened the beam to around 2 nm. The size of the final electron probe was around 3 nm. The step size for the ACOM-TEM image acquisition was 6 nm, the frame size 488 × 590 pixels, in order to reach a large mapping area comparable to the EFTEM-SI mapping.

Figure S 2a shows an example of a nano beam electron diffraction pattern from the ACOM-TEM data used in the current work. The small diffraction disks are the results of the convergence angle setup of the electron beam for nano beam diffraction. Matching of experimental diffraction pattern and simulated diffraction templates for the determination of crystal orientation and phase identification has been computed using the ACOM-TEM NanoMegas software package. The banks (database) of the diffraction templates have been calculated based on the olivine-type LFP and FP crystal structures with the axes defined as a = 10.329 Å, b = 6.006 Å and c = 4.691 Å for LFP and a = 9.814 Å, b = 5.789 Å and c = 4.782 Å for FP [22]. More details for the templates matching are described in the supplementary information section 2 (SI.2). The final orientation and phase data were imported into matlab and analyzed using MTEX 4.1 [23] for quantification of the misorientation and orientation density.

2.3 EFTEM-SI

EFTEM-SI and STEM-EELS-SI data for determining the LFP/FP phase maps were acquired using an aberration (image) corrected Titan 80-300 (FEI Company) operated at 300 kV, equipped with a GIF tridium spectrometer with a BM-UltraScan CCD camera. For the acquisition of the EFTEM-SI, a µp EFTEM setup was used with a frame size of 512 × 512 pixels and a pixel size of 6.13 nm. To determine the LFP and FP phases, two different regimes for the EFTEM-SI are available: at high energy loss, i.e. Fe-L_3 edge with an onset at 708 eV, and at low energy loss from 0 to 75 eV including interband transitions (4 to 20 eV), volume plasmon (20 to 30 eV) and Li-K/Fe-M edge (55 to 70 eV). For the acquisition in case of Fe-$L_{3,2}$ edges, we adopted the settings suggested by Sugar et al. [11]. As measuring condition a 4 eV energy slit and an energy shift step of ΔE = 1 eV per image with an exposure time of 120 s per image were applied. The energy range was set from 696 eV to 735 eV (40 images). A 40 µm objective aperture was selected. In case of the low-loss regime, a 1 eV energy slit and a shift step of ΔE = 0.5 eV per image were applied. The acquired energy range was from -4 eV to 80 eV. The acquisition time was 4 × 1 s per image from -4 eV to 50 eV and 24 s per image from 50 eV to 80 eV. A 20 µm objective aperture was used for reducing the effect of multiple inelastic-scattering and coevally increasing the energy resolution. The details for the STEM-EELS-SI acquisition are described in the supplementary information section (SI.3).

3. Results and discussion

3.1 ACOM-TEM and EFTEM-SI Fe-L_3 mapping of the LPF/FP phase distribution

Figure 1a shows an ACOM-TEM phase map on the half lithiated specimen (green: $LiFePO_4$, red: $FePO_4$) according to the crystallographic difference between $LiFePO_4$ and $FePO_4$. In agreement with Brunetti's work [12], the map indicates that large number of particles are either LFP or FP for the partially discharged material measured ex-situ, which implies a thermodynamically stable condition. In addition, quite a number of particles are observed with a typically well-defined boundary between LFP and FP. The crystal orientation map (figure 1b) shows that, while the overall particle orientation is fairly random, the nanoparticles typically exhibit a single crystallographic orientation with some slight internal orientation variations. This is also the case for particles with a mixed LFP/FP phase.

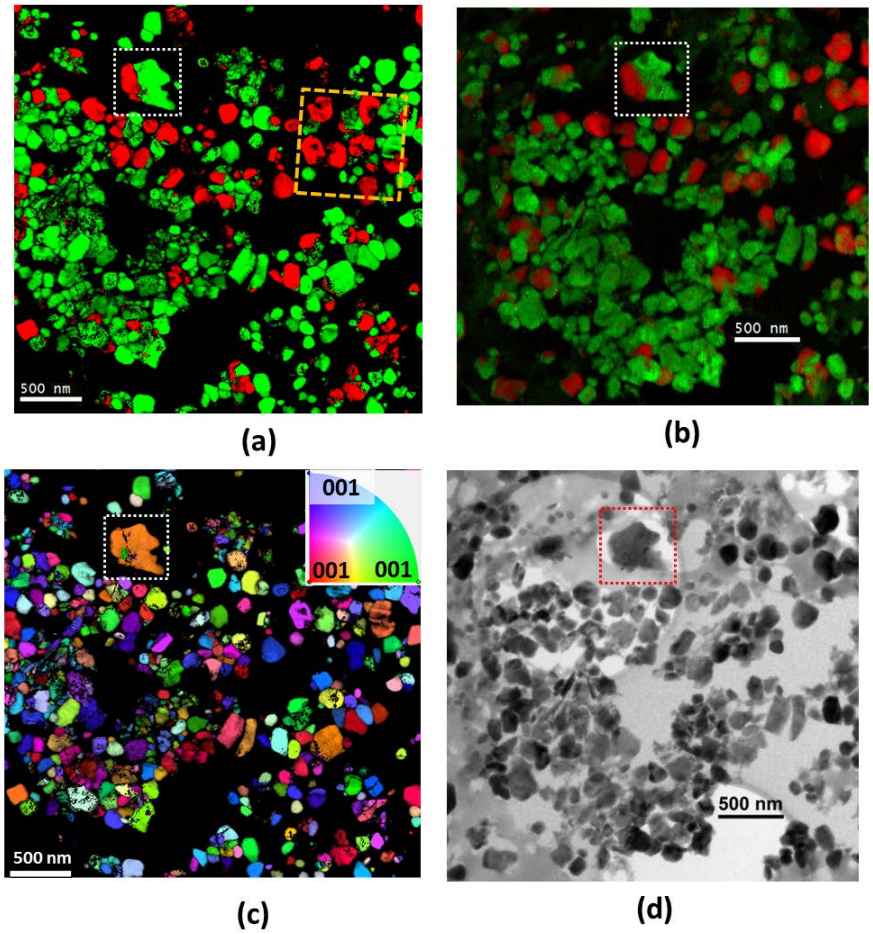

Figure 1 (a) ACOM-TEM Phase map of LFP (green) and FP (red) by the crystallographic difference between both. The orange box highlights the same area of phase map from STEM-EELS-SI in Figure S 3d. (b) Phase map obtained by EFTEM-SI at the Fe-$L_{3,2}$ edge (Fe valance state map) ($LiFePO_4$: green, $FePO_4$: red). (c) ACOM-TEM crystal orientation map. The inverse pole figure color coding is given to the right. (d) Bright-field image of the same area as **c**. The white boxes in a,b and c and the red box in d indicate same particle for visual guidance.

According to literature [7,11], an energy shift of around 1.8 - 2 eV exists for the Fe-L_3 edge in the Fe^{2+} state in LFP and the Fe^{3+} state in FP. As shown in Figure S 3a, we observed an energy shift of 1.8 eV in the current work. This significant energy shift offers an easy way to differentiate the Fe^{2+} and Fe^{3+} valance states, hence to distinguish the LFP and FP phases. In this work, the EFTEM-SI data cubes were analyzed by multiple linear least square (MLLS) fitting, which has been implemented in DigitalMicrograph™ as a standard plugin [24]. To calculate the phase map from the Fe-L_3 edge, linear combinations of two reference spectra taken from as-prepared LFP and fully charged FP (figure S 3a) were fitted to the acquired EFTEM-SI data cube at every pixel. The MLLS fitting calculates the 2D image as a combination of coefficients (figure S 3b and c) for each reference spectrum. The coefficient images are RGB color mixed and shown as phase map in figure 1b (green: $LiFePO_4$, red: $FePO_4$). The map is taken at (almost) the same location as the ACOM map. A BF-TEM image is given (figure 1d) as a reference.

The EFTEM-SI and ACOM-TEM phase maps in figure 1a and c show excellent agreement with each other. Differences can only be seen at the few pixel level as well as in the strength of the reliability/fitting coefficients (figure S 2f, g and figure S 3b, c). Furthermore, a map obtained by STEM-

EELS-SI at the Fe-L_3 edge (figure S 3d) agrees with both the ACOM-TEM (figure 1a) and the EFTEM-SI Fe-L map (figure 1b) in the area denoted by the orange boxes in figure 1a. All these prove the reliability of the ACOM-TEM and EFTEM/STEM-EELS (at the Fe-L_3 edge) phase analysis and hence prove the reliability of the two kinds of methods for LFP/FP phase mapping. A discussion of the success of the ACOM-TEM analysis is given in SI.2.

3.2 Crystallographic analysis of the ACOM-TEM data: properties of the internal phase boundary

The confirmation of the ACOM-TEM analysis by EFTEM phase mapping now allows for a more detailed analysis making use of the crystallographic information contained in the ACOM-TEM data set. In both, the ACOM-TEM and the EFTEM maps, we carefully checked and excluded any overlapping particles and non-monocrystalline nanoparticles with the help of the orientation map (figure 1c). Afterwards, we could confirm many individual nanoparticles with uniform single-crystal like orientation exhibiting both, LFP and FP phases, in agreement with published experimental observations [4,5,14,16] and theoretical modelling [25,26]. Some of the particles in figure 1a containing both phases are shown in detail in figure 2. It can be observed that in most cases the internal boundaries between the LFP and FP domains show a flat geometry. While it is difficult to directly correlate these observations with the boundary structure during cycling because of potential relaxation effects during the ex-situ analysis, it fits well to recent in-situ synchrotron X-ray diffraction studies [27] where a well-defined phase boundary has been observed during slow cycling (below C/2, close to thermodynamic equilibrium). In contrast, in kinematically controlled charging experiments, diffuse boundary structures have been reported [27,28]. The appearance of planar internal phase boundaries (IPB) suggests that the lithiation process under thermodynamic condition follows defined crystallographic directions and, furthermore, occurs as a correlated process and not randomly from the crystal surface. It reveals an energetic rule underlining the crystallographic property reported by the theoretical studies [25,26]. This rule perhaps also has influence to the relaxation of the reaction with non-equilibrium condition. Determining the orientation of the IPB is a key to explore the role of the crystallographic property on the electrochemical reaction. As the ACOM-TEM maps contain the complete orientation information, they offer the possibility to study the crystallography of the planar interfaces.

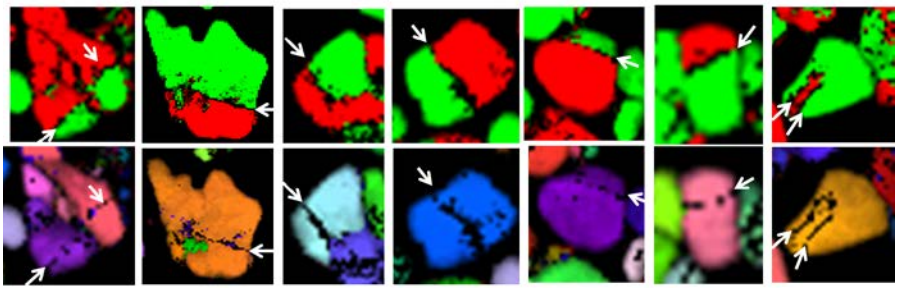

Figure 1 ACOM phase map (top) and orientation map (bottom) showing single-crystal-like nanoparticles (grains) containing two phases (not to scale). The flat internal phase boundaries are highlighted by white arrows.

3.2.1 Preferred orientations of IPBs from ACOM-TEM data

Data from more than 150 IPBs were detected in the ACOM-TEM maps. Neglecting too short (< 5 pixels, corresponding to 30 nm) and highly curved IPBs as well as strongly inclined IPBs with respect to the electron beam (detected by their broad interface with low reliability), finally 88 IPBs were selected for a statistical analysis of the preferential orientation. The orientations of these IPBs were extracted by fitting a linear function to the individual IPBs, calculating the normal of the line (IPB) and referring these sample-frame directions to the crystal orientations. The 88 orientations normal to the IPBs were then displayed in an inverse pole figure (figure 3a). As the IPBs are not necessarily oriented perfectly parallel along the viewing direction (electron beam), there will be some scatter of the measured IPB orientation. Nevertheless, from the IPB orientation distribution illustrated in figure 3a, and even more clearly in the calculated orientation density function (ODF) (figure 3b), one can recognize an overall tendency of a preferred IPB orientation. The red color in the ODF corresponds to the largest population of IPB orientations which is normal to [101] crystalline direction. It reveals the most preferred orientation of the LFP/FP interface consistent with the theoretical calculations [25,26]. However, the scatter in the data, even when considering deviations due to projection effects of some boundaries, is too much for a single orientation of all IPBs. In fact, a second local maximum with an IPB orientation close to [010] can also be recognized, while IPBs oriented along [001] have never been observed which is also in agreement with [25,26]. This clearly shows the need for a further statistical analysis of the ACOM-TEM data to develop an appropriate model for the IPBs.

3.2.2 Misorientation at IPBs

The epitaxial relationship at the IPBs is not only defined by the preferred orientation of the IPBs, but also lattice mismatch defects such as dislocations at the IPBs or lattice tilt are important as they may play a significant role in aging of intercalation materials in batteries. However, due to the beam sensitivity of LFP/FP, obtaining high quality HRTEM data is not straight forward. Alternatively one can gain knowledge of the mismatch by analyzing the misorientation of the epitaxial IPBs. With the orientation information from the ACOM-TEM data, a misorientation map around the IPBs can be calculated: The mean orientation of the single-crystalline phase with the largest area in a two phase particle is calculated. The misorientation of each pixel in the particle is then calculated as the angle between the local orientation of that pixel and the mean orientation. Typically, the misorientation between phases cannot be calculated if the phases are of different crystallographic structures. Here, both phases are the same apart from the lattice constants. Hence, both phases were assigned as one phase to detect slight orientation differences between them. Figure 3c shows the misorientation map calculated from the ACOM-TEM data in figure 1a. All single-phase particles are only outlined, while the misorientation is shown for all particles containing an IPB. Misorientation of 1 – 3° is revealed for all IPBs (red lines). In this work, this misorientation is also seen by HRTEM together with geometric phase analysis (GPA) for an individual boundary (figure S 4), which is consistent with previous HRTEM observations in [14,16]. A statistical analysis of the misorientation at the IPBs is computed from the orientation data and shown in figure 3d. The misorientation angle is on average 1.4°. One possible reason of the misorientation observed here is the lattice mismatch at the IPBs. The lattice mismatch in principle can be compensated by dislocations or by a tilt of the crystal orientation. Correspondingly, the misorientation (tilt of the crystal orientation) slightly reduces the dislocation density at the interface, which could help to reduce the crack formation on the nanoparticles and thus possibly contribute to the acknowledged excellent cycling stability of such olivine-type iron phosphate hosted nano-material [29–31]. Figure S 5 in the supplementary material shows the good charge/discharge cycling behavior of the LFP material used in this study.

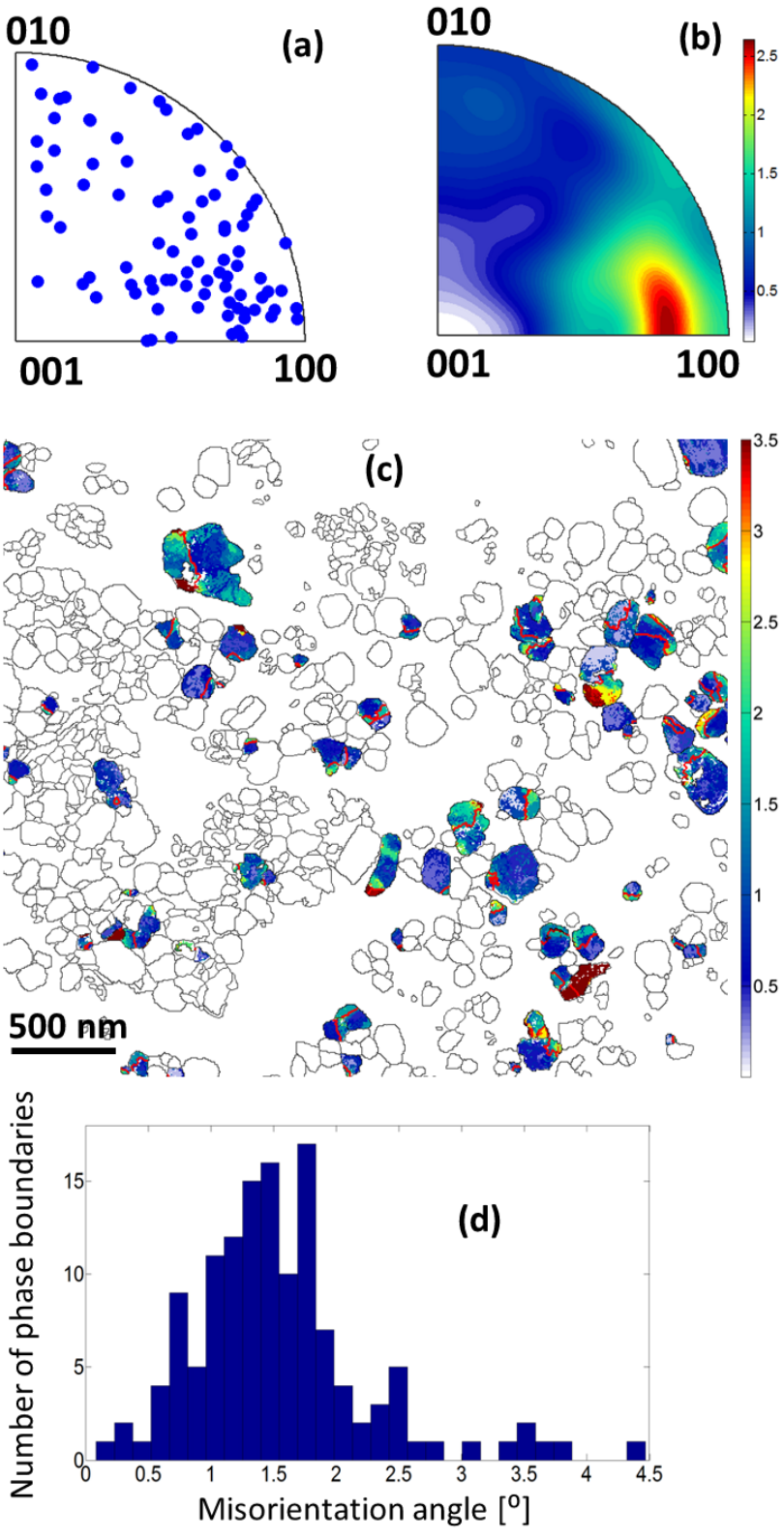

Figure 2 ACOM-TEM data analysis: (a) Inverse pole figure of the orientation normal to the (planar) internal phase boundaries. (b) Inverse pole figure of the orientation density function (ODF) of the planar internal phase boundaries calculated from the data shown in **a**. (c) Misorientation map: The color of each pixel corresponds to the misorientation angle between the orientation of the pixel and the mean orientation of the major phase in the two phase particle. (d) Misorientation histogram.

3.3 Fast mapping by EFTEM-SI at low-loss regime

Since ACOM-TEM phase mapping is based on a scanning strategy, its disadvantage is that it requires relatively long acquisition times for large frame sizes. With a 100 fps acquisition speed of the diffraction patterns and a frame size 500 × 500 pixels comparable to the EFTEM configuration, the total acquisition time is around 45 min. Such long acquisition times render the application of the phase mapping for in-situ cycling experiments difficult, as in-situ experiments often require fast recording time to image dynamic changes in the sample during a reaction. In contrast, EFTEM images record the information in parallel with large image frame sizes potentially reducing the acquisition time compared to scanning based techniques such as ACOM-TEM or STEM-EELS-SI. However, following the Boltzmann distribution, the inelastic cross-section exponentially decreases when increasing energy-loss. To record an EFTEM-SI map at the Fe-$L_{3,2}$ edges with an energy range of 696 - 735 eV requires long exposure times for each energy channel to obtain a reasonable signal to noise ratio even though they are white lines. In this work, acquisition times of 120 s per frame with a 4 eV slit width have been used. The total acquisition time was almost 1.5 hours. Even if only the Fe-L_3 edge is recorded from 696 eV to 720 eV, which would provide enough information to differentiate between LFP and FP, the total acquisition time would be 50 min. Thus, using a spectral feature that provides high intensity signals is interesting for in-situ work and to reduce the total dose. The following described three approaches based on EFTEM-SI at energy-losses below 80 eV provide the capability for fast phase mapping for LFP/FP.

3.3.1 Li-K and Fe-M edges

It has been demonstrated that it is possible to distinguish between LFP and FP based on the Fe-M edge at 55 eV which is overlapped with the Li-K edge [17,19]. The specimen prepared by ultramicrotomy is thin enough to render multiple scattering effects negligible. Two background subtracted spectra taken from LFP and FP particles (figure 4a) show significant difference from each other and provide a good signal to noise ratio for phase mapping. MLLS fitting is performed by taking the two spectra in figure 4a as references. A high quality phase map obtained by EFTEM-SI at Fe-M/Li-K (figure 4b) is in good agreement with the results previously obtained by ACOM-TEM and EFTEM-SI Fe-L_3. Images of the two fitting coefficients are shown in figure S 3e and f.

3.3.2 Interband transition

It has been reported [9,19] that a peak between the zero-loss and the plasmon peak associated to interband transitions exists in FP, but disappears in LFP, as shown in figure 4e, where the shoulder at 5 eV in the red curve taken from FP particles vanishes for the green curve of an LFP particle. Fast mapping of the delithiated state (FP phase) has been demonstrated by taking EFTEM images with an energy selecting slit at 5 eV [6,10,12]. However, variation of the contrast in the image could also be the result of thickness and excitation changes of the Bragg conditions when an objective aperture is used. Furthermore, both amorphous and graphitic carbons, either due to the embedding resin, the carbon support film or binders and electrical conductors mixed with the active material to enhance the electrical conductivity, also cause an energy-loss peak at around 5 eV, shown in figure 4e (the right shoulder of the zero-loss peak in the blue curve). Therefore simple imaging using the inelastically scattered electrons in an energy window of 3 - 7 eV cannot distinguish between FP and carbonaceous materials.

Calculations by Kinyanjui et al. [19] indicate significant differences in the conduction bands of LFP and FP, as FP is close to a Mott-Hubbard insulator, while LFP is a charge transfer insulator, as one more electron is added into the Fe 3d orbital after FP is lithiated to LFP. The interband transition

does not only generate the additional peak at 5 eV for the FP phase, but also causes strong differences in the dielectric function in the energy range from 0 eV to 20 eV for LFP and FP, especially the absorption function, i.e. the imaginary part (ε_2) of the dielectric function, as shown in figure 4c. Since the electronic structure of the carbonaceous materials is different from that of LFP and FP, the ε_2 of the carbonaceous material (Figure 4e, blue curve) is different from that of LFP and FP. Consequently, by characterizing the dielectric functions not only LFP and FP but also the carbon additives can be differentiated in a map.

The dielectric functions (3D data cube) were calculated by applying the Kramers-Kronig analysis embedded as a plugin in DigitalMicrograph™ to the data cube of the EFTEM-SI from -4 eV to 40 eV. Reference ε_2 functions (Figure 4c) were selected from pure LFP and FP particles as well as from the carbon support of the specimen according to the previous knowledge from the ACOM-TEM map. Distributions of LFP, FP and carbon are then computed by MLLS fitting of the reference ε_2 to the ε_2 data cube. The images of the fitting coefficients are shown in Figure S 6 a-c. The phase map is shown in Figure 4d, where only LFP and FP are displayed for better comparison with the other maps. Figure 4d exhibits a high quality for the phase determination. Nevertheless, a few slight artifacts caused by the correction procedure of the isochromaticity can be noted, e.g. the dark contrast in the particle highlighted in the white box.

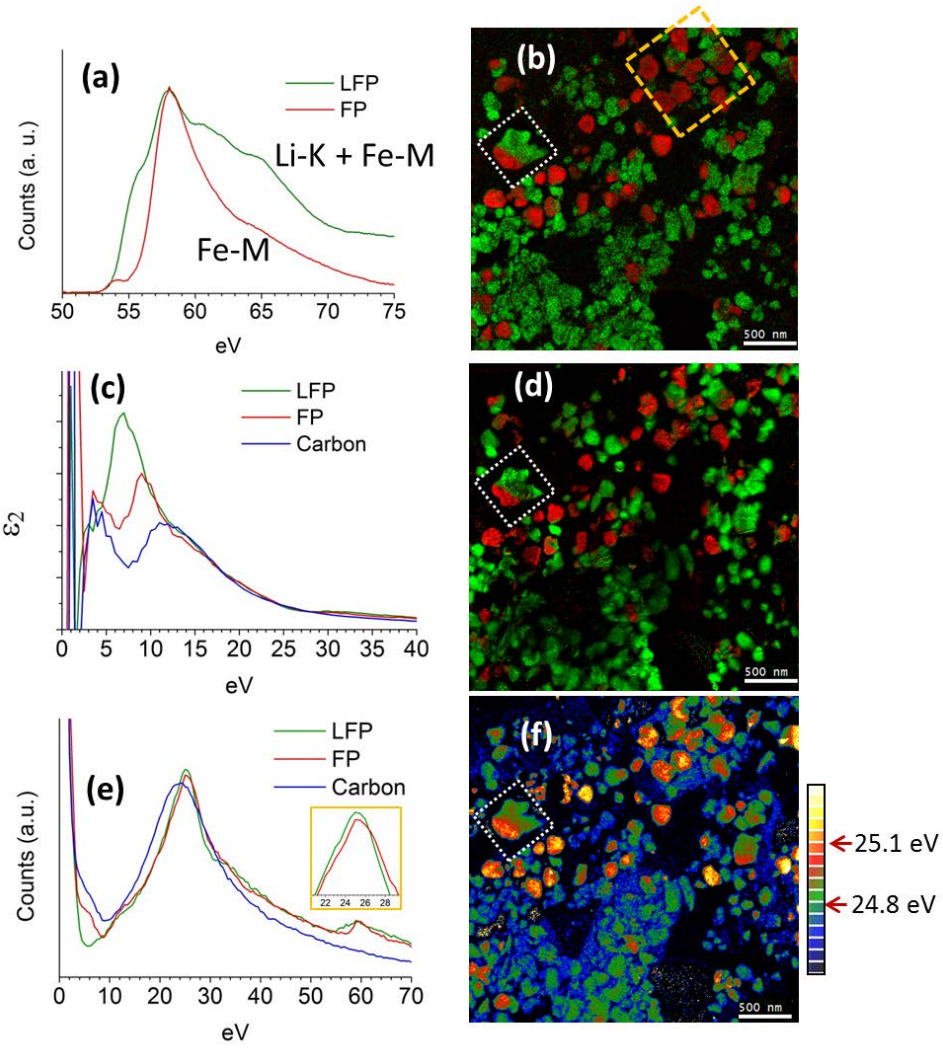

Figure 3 Phase maps by EFTEM-SI analysis and relating spectra at different energy ranges: (a) Illustration of the differences of the Li-K and Fe-M core-loss features for $LiFePO_4$ (green curve) and $FePO_4$ (red curve). (b) Phase map (green: $LiFePO_4$, red: $FePO_4$) obtained by EFTEM-SI at the Li-K and Fe-M range shown in **a**. (c) Dielectric functions (imaginary part) of $LiFePO_4$ and $FePO_4$ calculated from the EELS low-loss regime (-5 - 30 eV) by Kramers-Kronig analysis. (d) Phase map (green: $LiFePO_4$, red: $FePO_4$) obtained by differentiating the features of the imaginary part of the dielectric functions in c. (e) Low-loss spectra of $LiFePO_4$ (green curve), $FePO_4$ (red curve) and carbon (blue curve). The volume plasmon peaks are enlarged in the insert. (f) Volume plasmon center map. A color-bar is plotted at the right side, where 24.8 eV corresponds to the volume plasmon energy in LFP and 25.1 eV corresponds to the volume plasmon energy in FP. The boxes with white dashed-lines are to guide the eye comparing the features. They highlight the same particles indicated by the boxes in figure 1. The orange box in ***a*** highlights the region investigated by STEM-EELS in figure S 3***d***.

3.3.3 Volume plasmon

Figure 4e shows that the volume plasmon in FP (red curve) is shifted 0.29 eV to higher energy compared to that in LFP (green curve). A phase map can be then obtained by measuring the center of the volume plasmon peak. According to the non-linear least squares (NLLS) fitting [24], one can fit a Gauss function to the plasmon peak at each pixel in the EFTEM-SI series in the range between 23 eV to 28 eV, then the center of the volume plasmon at each pixel in the EFTEM-SI can be read out from the Gauss functions. An LFP/FP phase map is obtained which is color coded with the values of volume plasmon peak center (figure 4f). As shown in the color bar for figure 4f, areas in bright-red color have a higher plasmon energy corresponding to FP, while areas with color towards dark blue correspond to a low plasmon energy region, where green and bright blue indicate LFP and dark blue corresponds to the carbon support (from the TEM Cu grid) and embedding resin.

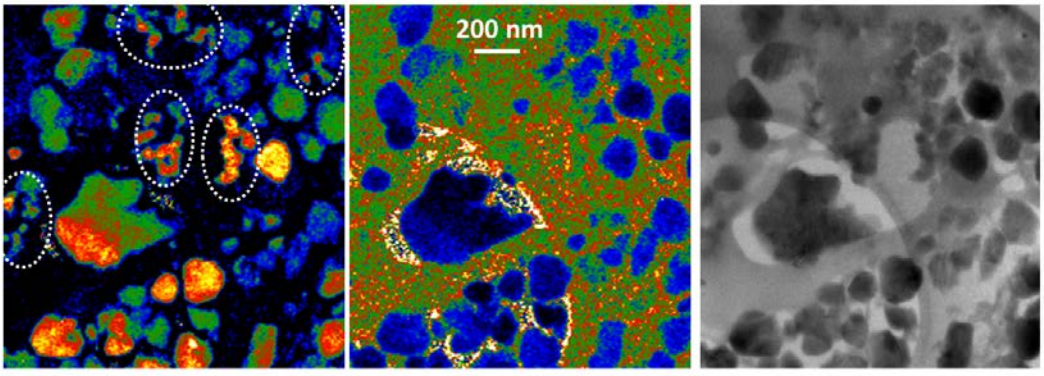

Figure 4. (a) Magnified plasmon-center map of figure 4f. (b) Map colored by value of full width half maximum of the volume plasmon peaks. (c) BF-image for comparison.

Different from the resin and the carbon support of the TEM grid, the graphitic carbon additives have a peak at higher energy in volume plasmon resonance. As shown in figure 5a (magnified from figure 4f), with the graphitic carbons highlighted by white dashed circles, the color corresponding to the graphitic carbon additives in the plasmon center map is in the color range between bright-red and green such as the active materials (LFP and FP) are. This confusion can be eliminated by comparing the plasmon center map (figure 5a) with a map showing the distribution of the full width at half maximum (FWHM) of the plasmon peaks (figure 5b). In the FWHM map, the LFP and FP particles appear blue, while all carbonaceous materials including both graphitic carbon and amorphous carbon are in the color range between red and green, because the FWHMs of their volume plasmon (> 14 eV) are significantly bigger than those of both LFP and FP (< 9 eV).

The situation is more complicated when the LFP/FP particles significantly overlap with the carbonaceous matrix. This overlap leads to an underestimate of the value of the volume plasmon center of the LFP/FP particles, resulting in a FP particle exhibiting LFP contrast. However, in the current case, we did not see this effect when the LFP/FP particles are noticeably larger than the thickness of the ultramicrotomed specimen. It can be seen that the phase map of particles larger than 100 nm in figure 4f is in very good agreement with the other maps. The mapping results can be further controlled by an accompanied elemental composition map of carbon and iron.

3.4 Comparison of the mapping methods

Five methods for LFP/FP phase mapping have been discussed in this work. They exhibit excellent consistency in terms of the measured phase distribution. The crystallographic and the energy loss spectroscopic analysis are in agreement for the LFP/FP system. It proves that all methods are reliable if the sample is sufficiently thin and uniform. Table 1 compares all the five methods in terms of acquisition time, dose and information content.

Table 1 Comparison of LFP/FP phase mapping methods in terms of acquisition dose, acquisition time and information contents

Methods	Energy range [eV]	Dose [$\times 10^5$ e·nm^{-2}]	Acquisition Time [min]	Information
Fe-L_3	696 – 720	16	50	Fe valance state
Li-K / Fe-M	50 – 66	4.2	13	Fe valance and Li environment
Kramers-Kronig analysis	-4 – 30	1.6	5	Dielectricity Optical properties
Plasma Center	23 – 28	0.31	< 1	Charge density
ACOM		3.7	45	Crystallography and Orientations relating to the phase interface
500 × 500 frame size (pixels) with around 6 nm resolution				

ACOM offers the option to work with relatively low dose and provides the best signal to noise ratio and is more tolerant to specimen thickness compared to the EFTEM methods when precession diffraction is used. In addition, the main advantage of ACOM-TEM is that it provides crystallographic information at each sampling point of the phase map. As demonstrated in section 3.2, lots of important information on the material properties can be extracted from the ACOM-TEM data, such as orientation distribution of internal LFP/FP interfaces and misorientation at the interfaces, as well as potentially also a strain distribution [32,33]. The acquisition time required for ACOM-TEM increases by a power of 2 with increasing frame size (number of pixels in the map). The acquisition of much larger maps is thus only possible for ex-situ experiments or using a high-speed camera.

EFTEM imaging of the energy shift of the Fe-L_3 edges (Fe valance state) offers good image quality, high reliability and a higher spatial resolution compared to ACOM (> 2-5 nm per pixel due to beam precession), especially when an chromatic aberration (C_c) correction is applied. However, this method requires both the longest acquisition time and highest electron dose. Thus, it is not promising for in-situ studies of the phase development during electrical cycling, because this requires both fast acquisition and low dose for less interaction between electron beam and the specimen.

The other three EFTEM methods using energy ranges below 66 eV require thinner specimens than ACOM or Fe-L EFTEM imaging as multiple scattering is more pronounced at low energy loss. However, the inelastic scattering cross-section in the low energy range, and hence the signal, is significantly

stronger compared to the Fe-L_3 edge with an onset at 708 eV. Therefore, they can provide LFP/FP phase maps in much shorter time and lower dose, as shown in Table 1. Especially the plasmon center determination is the fastest method with less than 1 min acquisition time and lowest dose (e.g. 12 times lower than that required for ACOM-TEM mapping). Although the plasmon center mapping has a potential limitation when examining particles smaller than the specimen thickness due to overlap with carbonaceous material, the plasmon center determination is a promising candidate for in-situ studies of the phase development during cycling of the LFP material because of the low dose and fast acquisition time.

4. Summary and conclusion

Five methods for LFP/FP phase mapping have been investigated and evaluated. By comparing the maps acquired at the same sample position, the excellent consistency provides strong evidence for the reliability of each method for uniform and thin samples.

ACOM-TEM based on scanning nano beam diffraction provides crystallographic information in addition to the phase maps. We demonstrated that statistical orientation information on the internal LFP/FP interface can be extracted from ACOM-TEM data. The other four methods are based on EFTEM-SI using the signals including the Fe-L edges, the Li-K/Fe-M edges, and the interband transitions analyzed by assistance of Kramers-Kronig relation as well as the volume plasmon resonance. The latter three only need short acquisition times and low electron doses, while still providing high quality maps. The plasmon center map has the fastest acquisition time with less than 1 min and works with much lower dose than others. It could be a possible candidate for LFP/FP phase mapping in in-situ studies of the phase evolution during electric cycling.

Acknowledgement

The authors would like to thank Prof. Max Fichtner for the fruitful discussions. XM and PN appreciate the financial support from the EU project Hi-C as part of the FP7 program under the project number 608575.

References

[1] W.C. Chueh, F. El Gabaly, J.D. Sugar, N.C. Bartelt, A.H. McDaniel, K.R. Fenton, et al., Intercalation pathway in many-particle LiFePO4 electrode revealed by nanoscale state-of-charge mapping, Nano Lett. 13 (2013) 866 – 872. doi:10.1021/nl3031899.

[2] Y. Li, F. El Gabaly, T.R. Ferguson, R.B. Smith, N.C. Bartelt, J.D. Sugar, et al., Current-induced transition from particle-by-particle to concurrent intercalation in phase-separating battery electrodes., Nat. Mater. 13 (2014) 1149–56. doi:10.1038/nmat4084.

[3] D.A. Shapiro, Y.-S. Yu, T. Tyliszczak, J. Cabana, R. Celestre, W. Chao, et al., Chemical composition mapping with nanometre resolution by soft X-ray microscopy, Nat. Photonics. 8 (2014) 765–769. doi:10.1038/nphoton.2014.207.

[4] Y. Li, S. Meyer, J. Lim, S.C. Lee, W.E. Gent, S. Marchesini, et al., Effects of Particle Size, Electronic Connectivity, and Incoherent Nanoscale Domains on the Sequence of Lithiation in LiFePO4 Porous Electrodes., Adv. Mater. 27 (2015) 6591–7. doi:10.1002/adma.201502276.

[5] Y.-S. Yu, C. Kim, D. a Shapiro, M. Farmand, D. Qian, T. Tyliszczak, et al., Dependence on Crystal Size of the Nanoscale Chemical Phase Distribution and Fracture in Li_xFePO_4., Nano Lett. 15 (2015) 4282–8. doi:10.1021/acs.nanolett.5b01314.

[6] D. Robert, T. Douillard, A. Boulineau, G. Brunetti, P. Nowakowski, D. Venet, et al., Multiscale phase mapping of LiFePO4-based electrodes by transmission electron microscopy and electron forward scattering diffraction, ACS Nano. 7 (2013) 10887–10894. doi:10.1021/nn4043964.

[7] L. Laffont, C. Delacourt, P. Gibot, M.Y. Wu, P. Kooyman, C. Masquelier, et al., Study of the LiFePO4/FePO4 two-phase system by high-resolution electron energy loss spectroscopy, Chem. Mater. 152 (2006) 5520–5529. doi:10.1021/cm0617182.

[8] Y. Honda, S. Muto, K. Tatsumi, H. Kondo, K. Horibuchi, T. Kobayashi, et al., Microscopic mechanism of path-dependence on charge–discharge history in lithium iron phosphate cathode analysis using scanning transmission electron, J. Power Sources. 291 (2015) 85–94. doi:10.1016/j.jpowsour.2015.04.183.

[9] W. Sigle, R. Amin, K. Weichert, P.A. van Aken, J. Maier, Delithiation Study of LiFePO4 Crystals Using Electron Energy-Loss Spectroscopy, Electrochem. Solid-State Lett. 12 (2009) A151. doi:10.1149/1.3131726.

[10] M.E. Holtz, Y. Yu, D. Gunceler, J. Gao, R. Sundararaman, K. a. Schwarz, et al., Nanoscale imaging of lithium ion distribution during in situ operation of battery electrode and electrolyte., Nano Lett. 14 (2014) 1453–9. doi:10.1021/nl404577c.

[11] J.D. Sugar, F. El Gabaly, W.C. Chueh, K.R. Fenton, T. Tyliszczak, P.G. Kotula, et al., High-resolution chemical analysis on cycled LiFePO4 battery electrodes using energy-filtered transmission electron microscopy, J. Power Sources. 246 (2014) 512–521. doi:10.1016/j.jpowsour.2013.08.003.

[12] G. Brunetti, D. Robert, P. Bayle-Guillemaud, J.L. Ouvi, E.F. Rauch, J.F. Martin, et al., Confirmation of the Domino-Cascade Model by LiFePO4 / FePO4 Precession Electron Diffraction, Chem. Mater. 23 (2011) 4515–4524. doi:10.1021/cm201783z.

[13] Y. Zhu, J.W. Wang, Y. Liu, X. Liu, A. Kushima, Y. Liu, et al., In situ atomic-scale imaging of phase boundary migration in FePO(4) microparticles during electrochemical lithiation., Adv. Mater. 25 (2013) 5461–6. doi:10.1002/adma.201301374.

[14] G. Chen, X. Song, T.J. Richardson, Electron Microscopy Study of the LiFePO4 to FePO4 Phase Transition, Electrochem. Solid-State Lett. 9 (2006) A295. doi:10.1149/1.2192695.

[15] L. Gu, C. Zhu, H. Li, Y. Yu, C. Li, S. Tsukimoto, et al., Direct observation of lithium staging in partially delithiated LiFePO 4 at atomic resolution, J. Am. Chem. Soc. 133 (2011) 4661–4663. doi:10.1021/ja109412x.

[16] C.V. Ramana, a. Mauger, F. Gendron, C.M. Julien, K. Zaghib, Study of the Li-insertion/extraction process in LiFePO4/FePO4, J. Power Sources. 187 (2009) 555–564. doi:10.1016/j.jpowsour.2008.11.042.

[17] P. Moreau, F. Boucher, Revisiting lithium K and iron M 2,3 edge superimposition: The case of lithium battery material LiFePO 4, Micron. 43 (2012) 16–21. doi:10.1016/j.micron.2011.05.008.

[18] M.E. Schuster, D. Teschner, J. Popovic, N. Ohmer, F. Girgsdies, J. Tornow, et al., Charging and discharging behavior of solvothermal LiFePO4 cathode material investigated by combined EELS/NEXAFS study, Chem. Mater. 26 (2014) 1040–1047. doi:10.1021/cm403115t.

[19] M.K. Kinyanjui, P. Axmann, M. Wohlfahrt-Mehrens, P. Moreau, F. Boucher, U. Kaiser, Origin of valence and core excitations in LiFePO(4) and FePO(4)., J. Phys. Condens. Matter. 22 (2010) 275501. doi:10.1088/0953-8984/22/27/275501.

[20] E.F. Rauch, J. Portillo, S. Nicolopoulos, D. Bultreys, S. Rouvimov, P. Moeck, Automated nanocrystal orientation and phase mapping in the transmission electron microscope on the basis of precession electron diffraction, Zeitschrift Fur Krist. 225 (2010) 103–109. doi:10.1524/zkri.2010.1205.

[21] E.F. Rauch, L. Dupy, Rapid spot diffraction patterns identification through template matching, Arch. Met. Mater. 50 (2005) 87–99.

[22] A.S. Andersson, B. Kalska, L. Haggstrom, J.O. Thomas, Lithium extraction/insertion in LiFePO4: An X-ray diffraction and Mössbauer spectroscopy study, Solid State Ionics. 130 (2000) 41–52. doi:10.1016/S0167-2738(00)00311-8.

[23] F. Bachmann, R. Hielscher, H. Schaeben, Texture Analysis with MTEX – Free and Open Source Software Toolbox, Solid State Phenom. 160 (2010) 63–68. doi:10.4028/www.scientific.net/SSP.160.63.

[24] Gatan, DigitalMicrograph EELS Analysis User's Guide, 2003.

[25] D.A. Cogswell, M.Z. Bazant, Coherency strain and the kinetics of phase separation in LiFePO4 nanoparticles., ACS Nano. 6 (2012) 2215–25. doi:10.1021/nn204177u.

[26] M. Welland, D. Karpeyev, D. O'Connor, O. Heinonen, Miscibility Gap Closure, Interface Morphology, and Phase Microstructure of 3D LixFePO4 Nanoparticles from Surface Wetting and Coherency Strain, ACS Nano. 9 (2015) 9757–9771. doi:10.1021/acsnano.5b02555.

[27] X. Zhang, M. van Hulzen, D.P. Singh, A. Brownrigg, J.P. Wright, N.H. van Dijk, et al., Direct view on the phase evolution in individual LiFePO4 nanoparticles during Li-ion battery cycling., Nat. Commun. 6 (2015) 8333. doi:10.1038/ncomms9333.

[28] H. Liu, F.C. Strobridge, O.J. Borkiewicz, K.M. Wiaderek, K.W. Chapman, P.J. Chupas, et al., Capturing metastable structures during high-rate cycling of $LiFePO_4$ nanoparticle electrodes., Science. 344 (2014) 1252817. doi:10.1126/science.1252817.

[29] F. Yu, L. Zhang, Y. Li, Y. An, M. Zhu, B. Dai, Mechanism studies of LiFePO 4 cathode material: lithiation/delithiation process, electrochemical modification and synthetic reaction, RSC Adv. 4 (2014) 54576–54602. doi:10.1039/C4RA10899J.

[30] S.-Y. Chung, J.T. Bloking, Y.-M. Chiang, Electronically conductive phospho-olivines as lithium storage electrodes., Nat. Mater. 1 (2002) 123–8. doi:10.1038/nmat732.

[31] J.W. Fergus, Recent developments in cathode materials for lithium ion batteries, J. Power Sources. 195 (2010) 939–954. doi:10.1016/j.jpowsour.2009.08.089.

[32] J.L. Rouviere, A. Béché, Y. Martin, T. Denneulin, D. Cooper, Improved strain precision with high spatial resolution using nanobeam precession electron diffraction, Appl. Phys. Lett. 103 (2013) 241913. doi:10.1063/1.4829154.

[33] P. Favia, M. Bargallo Gonzales, E. Simoen, P. Verheyen, D. Klenov, H. Bender, Nanobeam Diffraction: Technique Evaluation and Strain Measurement on Complementary Metal Oxide Semiconductor Devices, J. Electrochem. Soc. 158 (2011) H438. doi:10.1149/1.3546851.